Unified Reduced Model for a Dual Control Scheme of the High-Speed Response Brushless Excitation System of Synchronous Generators

Jonas Kristiansen Nøland, *Membership*, Erick Fernando Alves, *Senior Membership*,
Atila Pardini and Urban Lundin

***Abstract*—Developments of the high-speed response brushless excitation systems (HSRBESs) are ongoing in the power industry. This is because the transient response of the excitation system (ES) is a key performance indicator for the grid owner. In dealing with this problem, accurate prediction and control of the ES ceiling voltage are desirable. However, the brushless exciters' non-linear armature reaction causes the ceiling voltage to be unknown under varying operating conditions. This paper proposes a numerical average-value model (AVM) that captures all the main dynamics of the HSRBES. It is shown that the AVM relationships can be utilized for online prediction of the ceiling voltage and employed in a dual control scheme. The proposed model is validated against a dynamic voltage buildup test. Moreover, it is derived from a detailed model which is verified from instantaneous field measurements and further from finite element analysis (FEA). Finally, the accuracy and effectiveness of the AVMs' transient relationships proves the feasibility of the proposed dual control scheme and shows that it can be easily implemented in existing systems.**

***Index Terms*—Automatic voltage control, average-value model (AVM), brushless exciters, excitation systems, impedance characterization, standardization.**

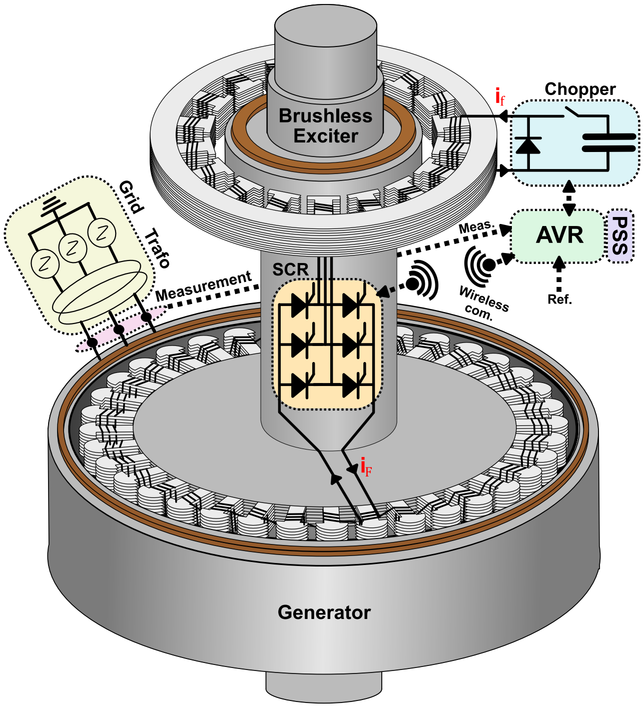

Fig. 1. Illustration of the overall system considered in this contribution.

I. INTRODUCTION

BRUSHLESS excitation systems (ESs) are employed in a wide range of applications for synchronous machines, such as nuclear power plants [?], [?], hydro power plants [?], aircraft power generation [?], [?], [?], shipboard power systems [?], vehicle traction [?], [?], and small-to-medium size generator sets [?], [?], [?]. Among the main reasons for their popularity are compact solutions, low maintenance, spark- and carbon dust free operation.

Several active control interfaces of rotating rectifiers in brushless ESs are proposed [?], [?], with some having similar or superior performance when compared to static ESs. Among them, the high-speed response brushless excitation system (HSRBES) is of particular interest, as this has been an off-the-shelf product for some years, and large synchronous generators are already adopting this technology [?], [?]. Fig. **??** illustrates this setup, which is implemented with a rotating thyristor rectifier in the rotor circuitry, replacing the passive diode bridge rectifier of a traditional brushless solution. In this case, control of the exciter field winding can be combined with direct control of the rotor circuitry through wireless communication. The active switching of the rotating thyristor rectifier and the stationary chopper, combined with the exciter machine saliency, makes model development of the HSRBES a complex task in comparison with other ESs [?]. The main challenge is the non-linear armature reaction that causes the ceiling voltage to be unknown and variable under changing loading conditions. This uncertainty demands ceiling voltage prediction and a new dual-control scheme in order to provide a reliable dynamic performance for grid applications.

A number of contributions have solved the most demanding challenges for efficient modeling of thyristor rectification systems [?], [?], [?], [?]. In addition, numerical average value-models (AVMs) have been proposed for the conventional brushless ES with rotating diode rectifiers [?], [?], [?]. Nowadays, AVMs are being proposed for improved control of brush-

Manuscript received November 5, 2018; revised May 15, 2019; accepted July 6, 2019.

less exciters in starter-generator applications [**?**]. However, the HSRBES has not yet taken the advantages of these techniques.

For the HSRBES, there is an interfacing challenge between the thyristor rectifier and the highly inductive generator field winding. The latter cannot be represented as an LC filter, where a steady state capacitor voltage is given. A method was recently proposed to directly interface with inductive circuitry [**?**]. This approach cannot be used for this particular application, since the proposed AVM relationships would strongly depend on the firing angle of the thyristor bridge. Moreover, previous approaches characterized only the positive quadrant of the thyristor bridge for an LC-type load [**?**], which is not sufficient for ESs.

This paper extends the AVM of the conventional brushless exciter [**?**] for the HSRBES. A careful selection of the dynamic impedance makes the AVM independent of the non-linear effects of the thyristor bridge firing angle, which solves the interfacing challenge of AVMs representing the HSRBES. The main contributions are the following:

1) The proposed numerical AVM allows unified modeling of the rotating thyristor rectifier of the HSRBES for all possible steady state and transient firing angles, which is a step necessary to develop standard industry models.
2) The look-up tables describing the relationships in the AVM provide the accuracy and precision required for implementation in the automatic voltage regulator (AVR), including
   - firing angle and zero crossing estimation, and
   - positive and negative ceiling voltage estimation.
3) The proposed AVM is used to develop a dual control scheme that includes direct control of the ceiling voltage. The performance of the proposed ceiling factor regulation (CFR) is compared against the conventional field current regulation (FCR) of the exciter. A case study is provided.

In addition to the already mentioned contributions, the dual control scheme is shown to indirectly control the steady state firing angle of the thyristor rectifier. In fact, firing angle restrictions in industrial solutions are needed to limit the exciter torque pulsations [**?**], [**?**]. As a result, this paper proposes a new control approach that can be directly applied to the existing conventional systems with minor modifications.

The rest of this paper is organized with the following structure. Section II specifies the investigated system, including key quantities. The proposed numerical AVM is presented in Section III, before the system is characterized with respect to the proposed AVM in Section IV. Finally, the dynamic results of the proposed AVM and its applicability for a dual control is given in Section V, before conclusions in Section VI.

II. SPECIFICATION OF THE INVESTIGATED SYSTEM

Figs. **??** and **??** illustrate the studied HSRBES, while Table **??** presents the ratings and key design parameters of the generator and the exciter, and Table **??** the normalized standard parameters. The ratings from the exciters' manufacturer data (Table **??**) are provided for the old system employing a rotating diode bridge rectifier. In reality, the power factor of the HSRBES is significantly lower. This is because the exciters' desired ceiling voltage factor (CF) requires a firing delay angle to the thyristors. The CF will vary depending on the local grid code. As a result, the common practice for the HSRBES is providing the data sheet with diode operation of the thyristor bridge (i.e., 0° firing angle).

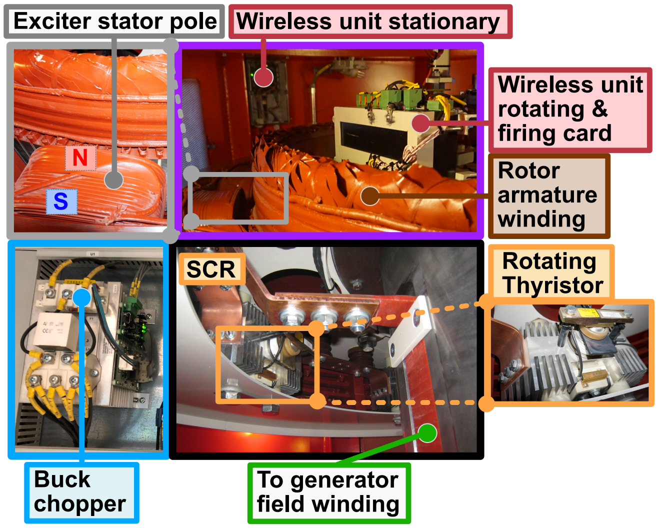

Fig. 2. Key components of the industrial test platform (Courtesy of *Voith Hydro AB* [**?**], [**?**]).

TABLE I
TEST SITE APPARATUS

Parameter	Description	Exciter	Generator	Unit
S	Apparent power	231	47 000	kVA
$\cos(\varphi)$	Power factor	$^{(1)}$0.919	0.900	
U	Terminal voltage	150	11 000	V
I_f , I_F	Rated field current	21.42	$^{(2)}$1156.00	A
n	Mechanical speed	166.67	166.67	r/min
f	Electrical frequency	25	50	Hz
p	Number of poles	18	36	
l_a	Active length	0.250	0.865	m
D_{si}	Inner stator diameter	1.71	6.42	m
D_o	Outer diameter	2.14	7.05	m
δ	Air gap length	5.3	18.0	mm
Q_r , Q_s	Number of slots	162	243	
q_r , q_s	Slots / (pole · phase)	3	2$^1/_4$	
c_r , c_s	Parallel circuits	6	1	
n_r , n_s	Conductors per slot	8	2	
	Armature winding	*wave*	*lap*	
n_d , n_D	Damper bars per pole	0	4	
n_f , n_F	Field turns per pole	240	26$^1/_2$	

1) Power factor given for rated rotating diode bridge operation, which is the standard specification for both the traditional exciters and the HSRBES.
2) Note that the exciter delivers the field current to the generator.

Fig. **??** shows the characteristic curves of the machines. Observe that the exciter does not saturate before two times the rated armature voltage. In addition, the Potier characteristics (green curve) of the exciter (Fig. **??**) is less saturated for higher exciter field current values. This is an approximation of the exciter armature voltage at rated load, i.e., it corresponds to full rated armature current in the d-axis. The approximation is valid because the loading condition is highly dominated by the d-axis armature current when the exciter is operating at high firing angles, which is typical for the HSRBES.

The open-circuit (OC) curves were identified by measuring

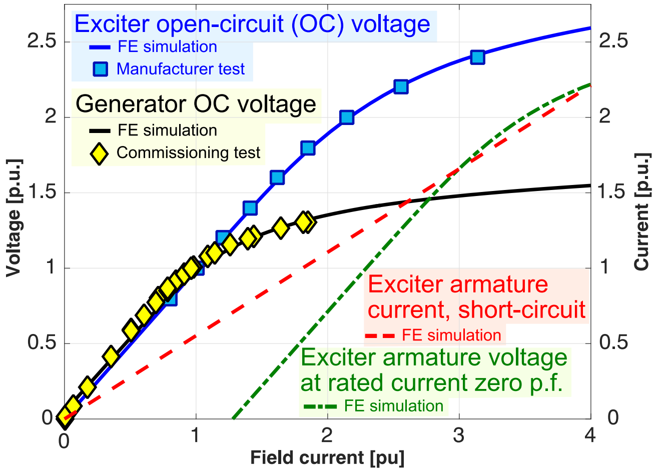

Fig. 3. No-load profile of brushless exciter and generator. Comparison between FE simulation and measurements. In addition, short-circuit and Potier characteristics of the brushless exciter. Field current in per unit corresponds to nominal armature voltage under no-load, $9.6\,\mathrm{A}$ for exciter and $594\,\mathrm{A}$ for generator.

TABLE II
MANUFACTURER STANDARD PARAMETERS

Parameter	Description	Exciter	Generator	Unit
X_d	D-axis reactance	1.912	0.959	pu
X'_d	D-axis trans. react.	0.410	0.299	pu
X''_d	D-axis subtrans. react.	0.390	0.198	pu
X_q	Q-axis reactance	0.883	0.687	pu
X''_q	Q-axis subtrans. react.	0.883	0.243	pu
X_l	Leakage reactance	0.212	0.170	pu
T'_{do}	Open-circuit time const.	2.113	5.309	s
T'_d	Short-circuit time const.	0.453	1.614	s

TABLE III
EXCITER EQUIVALENT CIRCUIT PARAMETERS AND GENERATOR FIELD WINDING PARAMETERS

L_d	$1.1856\,\mathrm{mH}$	L'_d	$0.2542\,\mathrm{mH}$
L_{md}	$1.0541\,\mathrm{mH}$	L_q	$0.5475\,\mathrm{mH}$
L_{fd}	$1.1931\,\mathrm{mH}$	L_{lfd}	$0.1390\,\mathrm{mH}$
R_a	$3.1071\,\mathrm{m\Omega}$	R_{fd}	$0.5646\,\mathrm{m\Omega}$
k_f	0.0105	R_f	$5.0887\,\Omega$
L_f	$10.7524\,\mathrm{H}$	M_f	$0.1004\,\mathrm{H}$
L_F	$0.595\,\mathrm{H}$	R_F	$0.1145\,\Omega$

the terminal voltage at different magnitudes of the field current. The same procedure applies for both the exciter and the generator, except that the armature voltages of the exciter were measured at the rotor side (inside-out synchronous machine). The FE simulation were made in 2D for both the generator and the exciter. Fig. **??** indicates a good agreement between the FE results and the commissioning tests.

III. PROPOSED NUMERICAL AVERAGE-VALUE MODEL

A. Detailed model formulation

The detailed model of the brushless exciter is formulated by three governing equations

$$u_d = -R_a i_d + \omega L_q i_q - L_d \frac{di_d}{dt} + L_{md}\frac{di_{fd}}{dt}, \tag{1}$$

$$u_q = -R_a i_q - \omega L_d i_d - L_q \frac{di_q}{dt} + \underbrace{\omega L_{md} i_{fd}}_{e_q}, \tag{2}$$

$$u_{fd} = R_{fd} i_{fd} + L_{fd}\frac{di_{fd}}{dt} - L_{md}\frac{di_d}{dt}, \tag{3}$$

where u_d and u_q are the d- and q-axis voltages (line-to-line rms), i_d and i_q are the d- and q-axis currents (in power-invariant scaling), L_d is the d-axis inductance, L_q is the q-axis inductance, L_{md} is the mutual d-axis inductance, L_{fd} is the field winding inductance, R_{fd} is the field winding resistance, u_{fd} and i_{fd} are the field winding voltage and current, and R_a is the armature resistance in the equivalent circuit of the exciter. All three equations interconnect with the rectifier interface feeding the generator field winding. The circuit parameters of the exciter are presented in Table III, which is calculated directly from the standard parameters of Table II. In particular, the generator field resistance (R_F) was derived from ohmic measurements at rated conditions and the OC field inductance (L_F) were calculated from $L_F = T'_{do} R_F$. A similar approach was employed in the characterization of the exciter as well.

The parameters of the detailed model must be validated before using them in the numerical AVM. The latter is generated by the post-processing of repeated detailed simulations. Therefore, an additional FE model is used to solve Eqs. **??**, **??** and **??** in the magnetic field domain and couples them directly with the thyristor rectifier that feeds the highly inductive field winding. In this simulation environment, the exciter field winding must to be voltage-sourced in order to accurately capture the commutation process by the FE model.

The final results are presented in Section IV, where the detailed model (with equivalent circuit parameters of Table III) and the FE model outputs are compared. In this context, the FE model is aimed to justify the validity of equivalent circuit parameters in Table III, and confirm the formulation of the detailed model along with the measured outputs outputs at the test site. In addition, it is aimed to show that the 3D effects are insignificant from a modeling perspective.

The exact shape of the no-load voltage behind the exciter reactance was not accessed from the test site. However, it was validated from the FE model to justify the sinusoidal shape approximation of the no-load armature line-voltage in the detailed model (results presented in Section IV-A and Fig. **??**).

B. AVM formulation

There is a fundamental difference between the detailed model and the proposed AVM. The AVM reduces all ac variables to be fundamental values and the dc variables to be averaged quantities (moving local average one-sixth of an electrical period). The AVM is formulated by three algebraic functions, which must be extracted from detailed simulations. The procedures that collects the functions as lookup tables are described in Section IV.

The first look-up table in the AVM assumes that there is a relationship between the fundamental ac voltage and mean dc

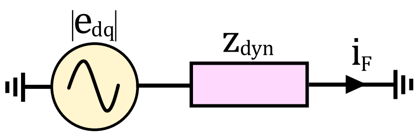

Fig. 4. Simplified characterization circuit valid for transient relationships.

voltage of the exciter, yielding

$$u_F = |u_{dq}| w_{uf}(z_{dyn}, \alpha), \tag{4}$$

where w_{uf} is an algebraic function (to be identified) depending on the thyristor bridge firing angle α and the dynamical impedance z_{dyn} (loading condition), and $|u_{dq}|$ is the fundamental component of the line-to-line armature voltage (rms) of the exciter. The loading condition is defined using the no-load voltage, $|e_{dq}|$ (voltage behind the reactances of the exciter armature), using a dynamic impedance (z_{dyn})

$$z_{dyn} = \frac{|e_{dq}|}{i_F}, \tag{5}$$

illustrated in Fig. **??**. It is worth mentioning that the intermediate variable z_{dyn} is necessary in order to fully account for the loading condition. Alternatively, using $|e_{dq}|$ alone yields a variable independent of the loading condition, i.e, it does not provide enough information to establish a dynamic relationship for the AVM. In addition, the terminal voltage, $|u_{dq}|$, and the output dc voltage, u_F, are highly dominated by the thyristor bridge firing angle, which must be decoupled from the intermediate variable to satisfy the AVM.

The proposed AVM includes power-invariant armature currents (i_d and i_q) that are formulated using algebraic functions, w_{id} and w_{iq} (to be identified), described by

$$i_d = \sqrt{3} i_F w_{id}(z_{dyn}, \alpha), \tag{6}$$

$$i_q = \sqrt{3} i_F w_{iq}(z_{dyn}, \alpha), \tag{7}$$

where $\sqrt{3}$ is a scaling factor since the functions are based on rms-values. The **????** means that there is a relationship between the averaged armature currents and the output dc current (i_F) of the exciter. The differentiation of i_d and i_q employs a low frequency approximation [**?**]. Finally, the armature voltages are continuously calculated from

$$u_d = -R_a i_d + \omega L_q i_q - L'_d \frac{di_d}{dt} + e_d, \tag{8}$$

$$u_q = -R_a i_q - \omega L_d i_d - L_q \frac{di_q}{dt} + e_q, \tag{9}$$

where the time-dependent no-load voltages are calculated from

$$e_d = \frac{L_{md}}{L_{fd}} (u_{fd} - R_{fd} i_{fd}), \tag{10}$$

$$e_q = \omega L_{md} i_{fd}. \tag{11}$$

The actual field quatities are given by $u_f = u_{fd}/k_f$ and $i_f = k_f i_{fd}$, where k_f is the reduction constant of the exciter field winding. The electromagnetic processes relating the different state variables are shown in Fig. **??**.

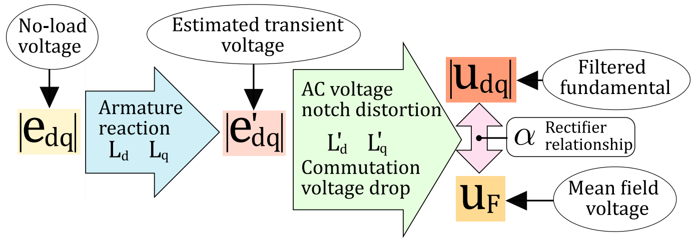

Fig. 5. Sketch of the processes related to the different state variables.

C. Stepwise overview of proposed AVM

1) The main generator model predicts the field current of the rotor poles, i_F. This paper utilized the synchronous machine model in the *Simscape Electrical* (formerly *SimPowerSystems*) environment of *MATLAB/Simulink*.
2) The exciter field current, i_{fd}, is a state variable in the automatic voltage regulator (AVR) system.
3) The exciter field voltage, u_{fd}, is a control variable from stationary part of the AVR system.
4) The instantaneous OC voltages, e_d and e_q, are calculated from eqs. **??** and **??**.
5) The dynamic impedance, z_{dyn}, is calculated as a ratio of magnitude of the OC voltage $|e_{dq}|$ and the generator field current i_F (Eq. **??**).
6) The exciter armature currents, i_d and i_q, are calculated from eqs. **??** and **??**, based on algebraic functions (w_{id}, w_{iq}), which appear as lookup-tables in the AVM.
7) A low frequency approximation [**?**] handles the calculation of $\frac{di_d}{dt}$ and $\frac{di_q}{dt}$ based on i_d and i_q as inputs.
8) The fundamental components of the exciter armature voltages, u_d and u_q, are calculated by eqs. **??** and **??**.
9) The output field voltage, u_F, is calculated from eq. **??**, where the algebraic function, w_{uf} (which is based on a lookup table), is multiplied with the magnitude of the armature voltage $|u_{dq}|$.
10) The rate of change of i_{fd} is integrated to obtain the input i_{fd} of the next time step of the simulation process (back to step 1). The rate of change in i_{fd} yields

$$\frac{di_{fd}}{dt} = \frac{L_d(u_{fd} - R_{fd} i_{fd}) + L_{md}(\omega L_q i_q - R_a i_d - u_d)}{L_{fd} L_d - L_{md}^2}. \tag{12}$$

The standard generator model does the same integration to reach the next step of the generator field current i_F, which goes back to the first step of the AVM structure (closed loop). The whole system is presented in Fig. **??**.

D. Ceiling factor estimator for the dual control scheme

The AVM and the dual control scheme of Fig. **??** can be used for implementing an online ceiling factor (CF) estimator based on 5 measured inputs (see Fig. **??**). The estimator calculates the positive ceiling voltage ($\widehat{u_F}$) based on the minimum firing angle (α_{min}) which is typically 10°. Eqs. 4, 5, 10 and 11 are implemented in the calculation. The CF

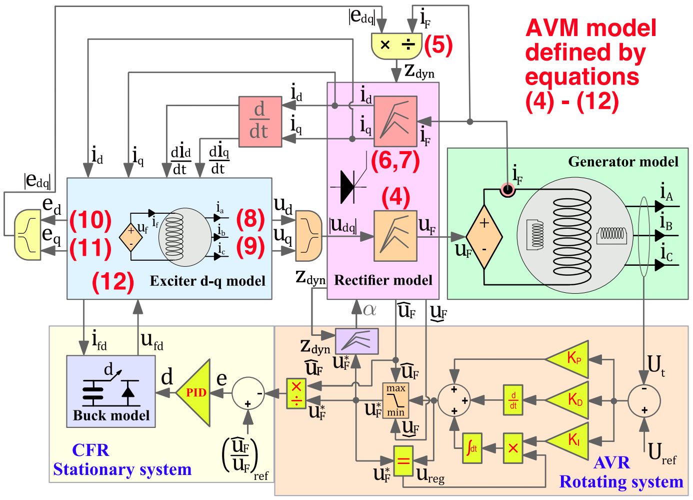

Fig. 6. Schematic illustration of the AVM model including the dual controller, i.e., by a CFR scheme of the exciter field winding.

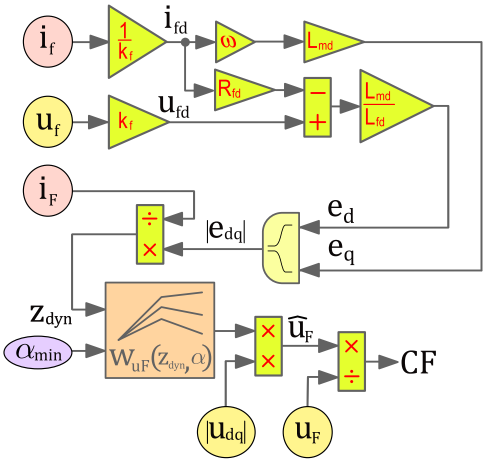

Fig. 7. The online CF estimator for the proposed dual control scheme utilizing eqs. 4, 5, 10 and 11. The input variables are u_f, i_f, u_F, i_F and $|u_{dq}|$. The output is the ceiling factor CF.

is defined as the ratio of $\widehat{u_F}$ and the actual field voltage (u_F) of the exciter, yielding

$$CF = \frac{\widehat{u_F}}{u_F}. \tag{13}$$

A similar approach could be used to estimate the negative ceiling voltage with the maximum firing angle (α_{max}) as input (150° is typical).

IV. CHARACTERIZATION OF THE HIGH SPEED RESPONSE BRUSHLESS EXCITATION SYSTEM

This section deals with the characterization of the brushless ES by means of the AVM in Section III.

A. Validation of the detailed model

Firstly, the detailed model must be verified against both experimental measurements and the FE model. Figs. **??** and **??** deals with the instantaneous armature line-voltage and the instantaneous output field voltage over an electrical time period.

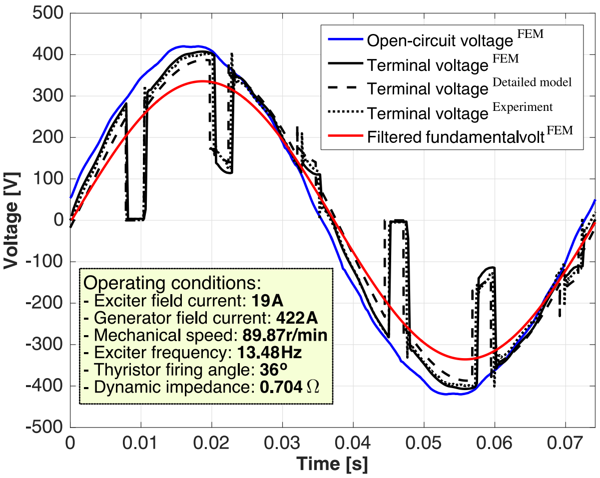

Fig. 8. Verification of rotor armature line voltage from site measurements, finite element method (FEM) and detailed model.

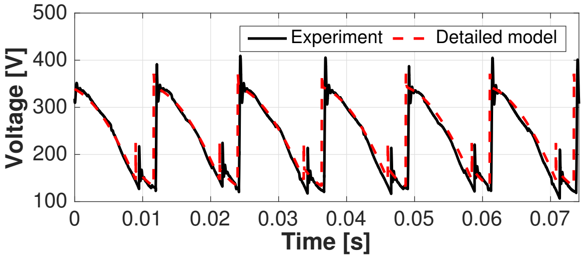

Fig. 9. Verification of output instantaneous field voltage by measurement. Same loading condition as Fig. 7.

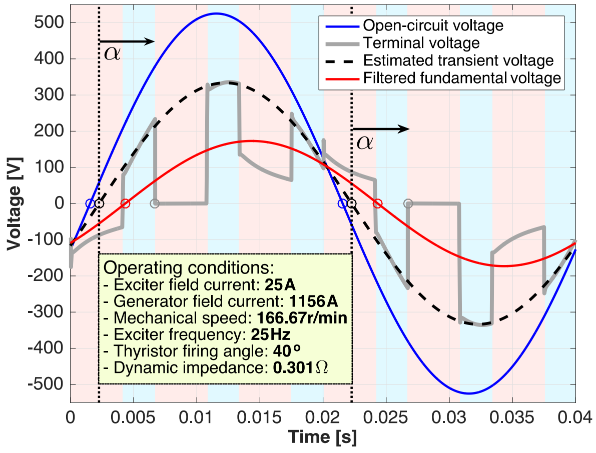

Fig. 10. Simulated zero-crossing for open-circuit voltage, terminal voltage, filtered terminal voltage and estimated transient voltage.

These measurements were extracted from another power plant with an identical exciter machine design (due to easier access for detailed measurements on the rotating side). However, the active length of this exciter was twice ($0.5\,\mathrm{m}$) and it was operated with a mechanical speed of $93.8\,\mathrm{r/min}$, or $56.3\,\%$ of the rated speed of the original (yielding $13.48\,\mathrm{Hz}$ electrical frequency). As a result, the no-load armature voltages and the

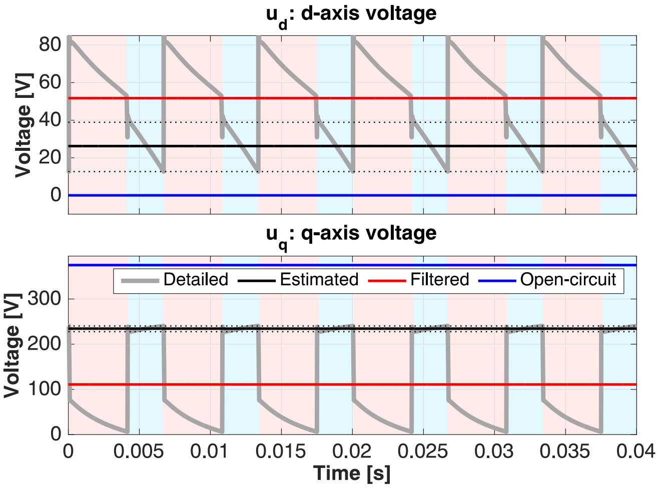

Fig. 11. D- and q-axis voltages simulated from the same loading condition as Fig. 9. The estimated transient d- and q-axis voltage components are highlighted in between the filtered and the open-circuit components.

machine reactance are about $12.5\,\%$ higher for this exciter, but the relative difference between the different parameters are identical, when neglecting the end-effects of the machine. It gave the opportunity for a detailed validation of the exciter, which is seen when comparing the FE model, the detailed model and the measurements shown in Fig. **??**. In addition, Fig. **??** illustrates the difference between the no-load armature voltage (from FE model), the actual armature voltage and the filtered armature voltage. The zero crossing of the filtered fundamental line-to-line voltage is slightly phase shifted with the true zero crossing. This phase shift delay will be even larger for higher loading conditions, and this is something the AVM will capture in the characterization process.

B. Firing angle prediction

Accurate firing angle detection of distorted line-to-line voltages for thyristor rectifiers has been addressed earlier [**?**], [**?**], [**?**]. Typically, the zero crossing is approximated from the OC line voltages or the filtered line voltages [**?**]. The OC zero crossing can be estimated by measuring the rotor position of the exciter. The true zero crossing lies in between these two methods. This paper removes the notches in the armature voltages by calculating the true zero crossing of the estimated transient armature line-to-line voltage (e'_{dq}). This is illustrated in Fig. **??**, which compares the proposed method with the alternative methods. The estimated e'_{dq} is calculated from the *dq* components of the terminal voltages. It is found by averaging the mean *d*- and *q*-axis voltages in the conduction interval (see Fig. **??**). Fig. **??** maps the difference between the filtered zero crossing and the estimated zero crossing proposed in this contribution. The proposed characterization technique replaces the conventional non-direct transfer functions to correct errors in the zero crossing detection applied in commercial systems.

C. Characterization of the detailed model

The validated detailed model was operated with different firing angles at different loading conditions by transient ramping of the output generator field current (i_F), which was emulated as a stiff current source during the characterization process. In fact, a stiff current source is a very good approximation when considering a highly inductive generator field winding. Fig. **??** shows the most valuable lookup tables from the simulated data. In particular, Fig. **??** a) shows a lookup table for prediction of the firing angle (α) for different transient loading conditions (defined by z_{dyn}) and different field voltages (u_F), with $w_{uF} = u_F/|u_{dq}|$ as the normalized input variable. This table yields a direct relation for estimation of the firing angle as a function of the desired output field voltage of the AVR under transient and steady state loading conditions (i.e., firing angle estimator). The reciprocal of the same lookup table is given in Fig. **??** b), were the firing angle (α) and dynamic impedance (z_{dyn}) are input variables. This is the parametric function utilized in the AVM **??**, which predicts the generator field voltage u_F. As mentioned in Section III-D, it is also possible to estimate the instantaneous positive and negative ceiling voltages as function of the loading condition with this table, by inserting the minimum and maximum firing angle (α_{min} and α_{max}) values as inputs. As a result, it can be used for implementation of variable saturation parameters inside the real AVR, for improved anti-windup performance.

Figs. **??** c) and **??** d) illustrate the ratio of the d- and the q-axis rms armature currents (i_d^* and i_q^*) to the generator field current (i_F), as a function of α and z_{dyn}. These are the parametric functions utilized in the AVM **????**, to predict the power-invariant d- and q-axis currents (i_d and i_q). In addition to the previous validations, all subfigures include an additional benchmark from ideal analytical solutions valid for ideal light load conditions (large dynamic impedance), given in Table **??**. The ideal analytical equations assumes instant commutation and square wave shaped armature currents.

TABLE IV
IDEAL ANALYTICAL SOLUTIONS AT LIGHT LOAD CONDITIONS

Coefficient	Analytical solution
$\alpha = \alpha\left(\frac{u_F}{\lvert u_{dq}\rvert}\right)$	$\alpha = \cos^{-1}\left[\frac{\pi}{3\sqrt{2}}\frac{u_F}{\lvert u_{dq}\rvert}\right]$
$w_{uF} = \frac{u_F}{\lvert u_{dq}\rvert}$	$u_F = \frac{3\sqrt{2}}{\pi}\lvert u_{dq}\rvert\cos(\alpha)$
$w_{id} = \frac{i_d^*}{i_F}$	$i_d^* = \sqrt{\frac{3}{2}}\frac{2}{\pi}i_F\cos(\alpha)$
$w_{iq} = \frac{i_q^*}{i_F}$	$i_q^* = \sqrt{\frac{3}{2}}\frac{2}{\pi}i_F\sin(\alpha)$

V. PERFORMANCE OF THE PROPOSED AVM

Finally, the proposed AVM was assessed with a dynamic test, in which the new CFR dual control scheme was evaluated.

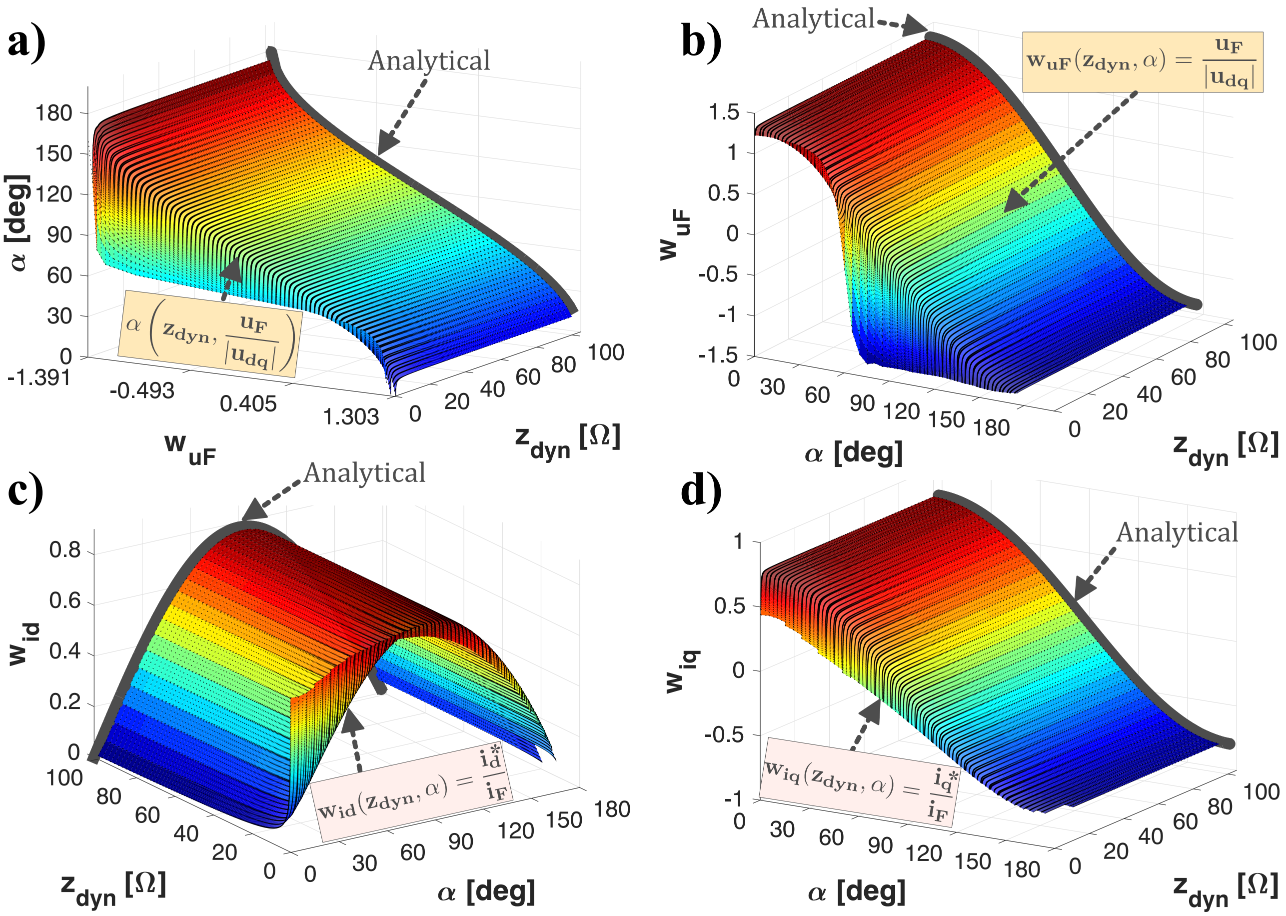

Fig. 12. Extracted parametric functions of the AVM ??????: **a)** $\alpha(z_{dyn}, w_{uF})$, **b)** $w_{uF}(z_{dyn}, \alpha)$, **c)** $w_{id}(z_{dyn}, \alpha)$, **d)** $w_{iq}(z_{dyn}, \alpha)$

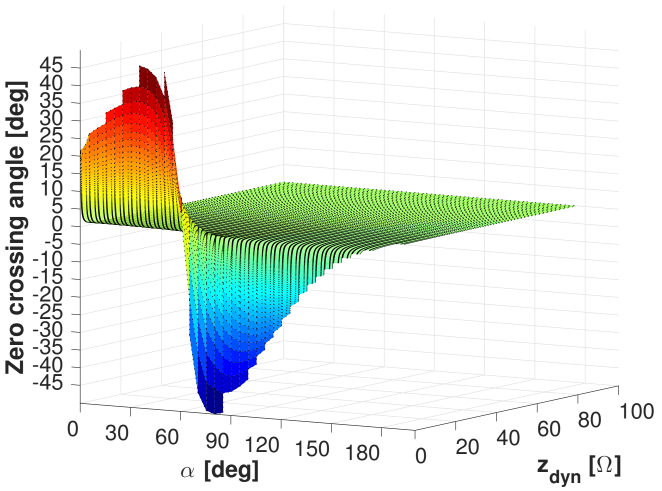

Fig. 13. The difference between the estimated zero crossing angle and the filtered zero crossing angle.

A. Dynamic voltage buildup test

Figs. 13-19 reveals the response of the key quantities of the ES during a dynamic voltage buildup of the generator (OC conditions). The initial armature voltage of both the exciter and the generator were initially at zero. The thyristor rectifier starts to act from 2 seconds after the start, and the whole time interval considered is lasting for 8 seconds. A comparison is made between; 1) the AVM; 2) The detailed model; 3) The local average of the detail model over one-sixth of an electrical period (avg.); 4) Experimental measurement. Local averaging is only needed for the quantities that are dominated by thyristor switching.

Fig. **??** assess the generator field winding quantities (u_F and i_F) and the thyristor bridge the firing angle (α). In this type of response, the generator field current and the generator terminal voltage are approximately equal. As expected, the ceiling voltage estimator (presented in Section III-D) tracks correctly the ceiling voltage factor during this response. The ceiling voltage is shown to be strongly influenced by the generator field current (i.e. it reaches a high value initially) and the CF stabilizes at 2 at the final steady state condition. In parallel to this response, the exciter field winding quantities (u_f and i_f) were measured and simulated (see Figs. **??** and **??**). Note that the control signal of the exciter field voltage (u_f) was utilized, i.e., employing FCR of i_f (Control parameters in Table V). The detailed buck chopper switching transients were neglected in the modeling due its relatively high switching frequency and due to the highly inductive nature of the exciter field winding. On the contrary, the exciter field current signature is dominated by the switching of the thyristor rectifier, which

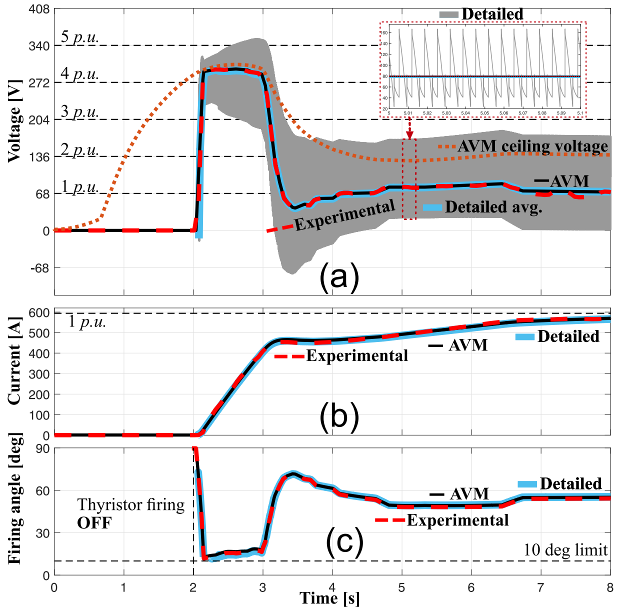

Fig. 14. Generator voltage buildup test: **(a)** Generator field voltage (u_F), **(b)** generator field current (i_F) and **(c)** thyristor bridge firing angle (α).

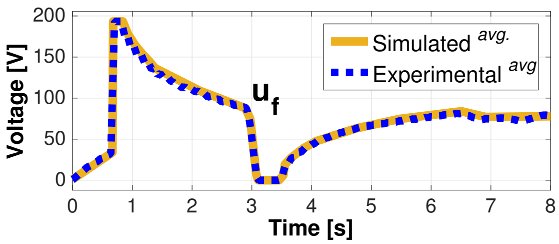

Fig. 15. Exciter field voltage (u_f) during the generator voltage buildup. The averaged field voltage control signal of the FCR is shown.

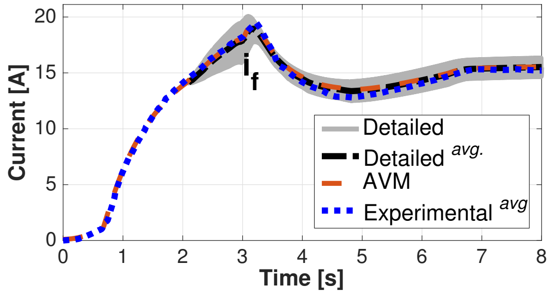

Fig. 16. Exciter field current (i_f) during the generator voltage buildup.

occurs between longer time intervals. As a result, they could not be neglected. However, the AVM is observed within the envelope of the exciter field current of the detailed model. A similar performance is observed in the the armature line-to-line voltage of the exciter in Fig. **??**. The notches due to commutation are shown in a zoomed view in Fig. **??**. Finally, the AVM d- and q-axis armature currents are assessed against the detailed model in Figs. **??** and **??**.

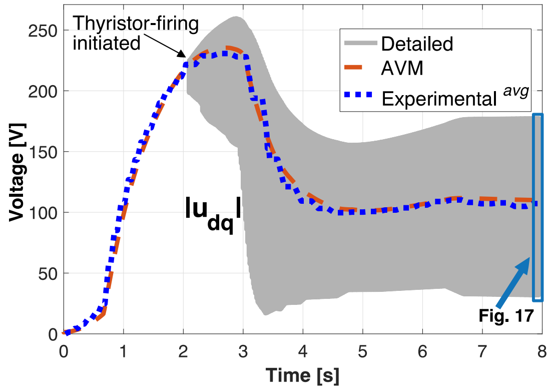

Fig. 17. Exciter armature voltage ($|u_{dq}|$) during the voltage buildup.

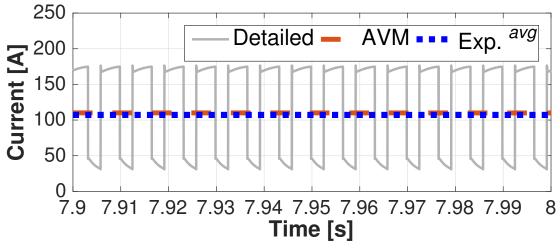

Fig. 18. Zoomed view of the exciter armature voltage of Fig. **??**.

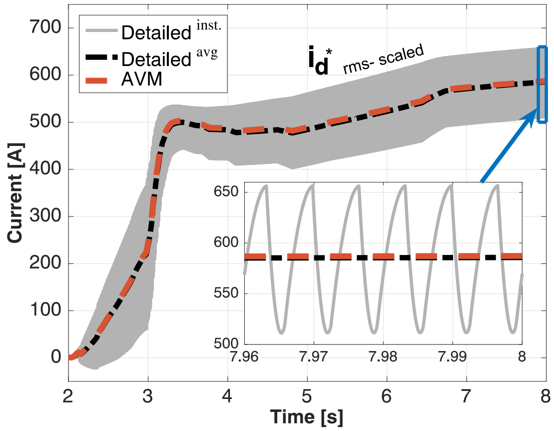

Fig. 19. Exciter d-axis armature current (rms) during voltage buildup.

B. Dual control methods evaluation and comparison

In the proposed dual control scheme (Fig. **??**), the main generators' AVR operates as a standard thyristor-based type AC4A model from IEEE 421.5 [**?**]. However, it is extended with an additional controller for the exciter CF, based on a CF estimator (Fig. **??**). ESs are typically verified by step responses under no-load conditions of the generator [**?**]. Fig. **??** shows how the proposed scheme behaves considering a 5 $\%$ step in the main generator's AVR set-point by applying different CFs. They are compared with a conventional control scheme, where the exciter field current is controlled to be constant. All settings

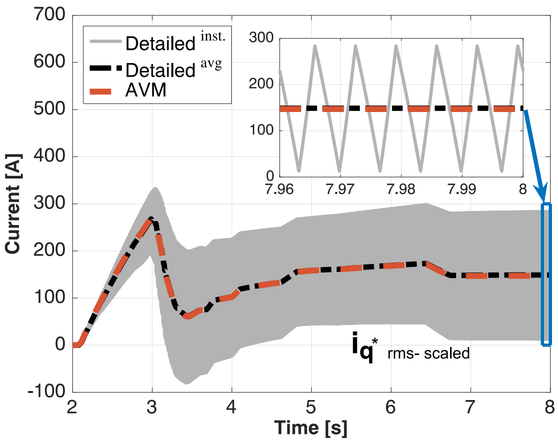

Fig. 20. Exciter q-axis armature current (rms) during voltage buildup.

TABLE V
CONTROL SETTINGS AND PERFORMANCE COMPARISON - 5% STEP

Control	**CFR**				**FCR**	**Unit**
Reference setting	$CF=$ 1.4	$CF=$ 1.6	$CF=$ 1.8	$CF=$ 2.0	$i_{fd}=$ 1.48	pu
k_p	44.7	39.1	34.8	31.3	35.6	pu/pu
k_i	111.7	97.8	86.9	78.2	12.4	pu/s
k_d	-0.254	-0.223	-0.198	-0.178	-0.223	pu · s
K_P	29.9	34.2	38.4	42.7	34.2	pu/pu
K_I	12.2	13.9	15.7	17.4	13.9	pu/s
Output	**CFR**				**FCR**	**Unit**
$i_{fd,1}$	13.07	13.98	14.79	15.58	13.98	A
$i_{fd,2}$	13.88	14.84	15.72	16.56	14.02	A
α_1	43.33	48.34	52.07	55.11	48.34	°
α_2	43.28	48.32	52.08	55.14	44.11	°
CF_1	1.40	1.60	1.80	2.00	1.60	pu
CF_2	1.40	1.60	1.80	2.00	1.43	pu
Rise time$^{(4)}$	0.452	0.366	0.309	0.271	0.385	s

1) k_p, k_i and k_d is the proportional, integrator and derivative coefficients of the exciter field winding regulator (CFR or FCR).
2) K_P and K_I is the regulator coefficients of the generator AVR.
3) Index 1 and 2 for the output means pre-value and post-value
4) Rise time means the time it takes to reach $90\,\%$ of the step value.

and performance comparisons are provided in Table V. The PID-regulator were appropriately tuned for each CF setting, in order to achieve the fastest $5\,\%$ AVR step response for each reference setting without overshoot. The dual control scheme recovers the initial ceiling voltage factor (CF), contrary to the conventional FCR scheme. The CF is highly correlated with the firing angle, which causes the proposed dual control scheme to indirectly control the steady state firing angle and consequently limit exciter torque pulsations [**?**], [**?**].

In Fig. 21, the conventional FCR scheme has an initial field current of $1.48\,\mathrm{pu}$, yielding an initial CF of $1.6\,\mathrm{pu}$. After the $5\,\%$ step change in the terminal voltage, the CF is reduced by $12.5\,\%$. It is evident that the CF becomes unstable, contrary to the proposed CFR scheme. Moreover, Fig. 19 shows that the CF is directly correlated with the speed of the response in the generator terminal voltage.

The existing practice of some suppliers to circumvent the apparent issues with the FCR, is to change the reference field current in discrete steps according to the main generator load (i.e., generator field current). Usually those transitions are chosen empirically. In this perspective, the FCR is chosen for its simplicity and the fact that it requires only one measurement. However, the ES cannot guarantee a required CF, which limits their application for large power generation facilities. On the contrary, the CFR requires 5 measured inputs, which are required to provide an accurate CF for the generator ES.

VI. CONCLUSION

This paper developed a numerical AVM of the HSRBES. The AVM was validated with experimental measurements, analytical solutions and FEA, and captures the key quantities in the exciter under stationary and transient conditions. As presented in this contribution, the proposed AVM can be utilized for online prediction during operation of the HSRBES to instantaneously estimate the ceiling voltage and the zero crossing error in the fundamental component of the line-to-line voltages. The AVR could take advantage of the proposed AVM to solve the following.

1) The proposed CFR ensures the speed-of-response by maintaining the CF under changing loading conditions, as well as maintaining the steady state firing angle;
2) Continuously estimate the positive and negative saturation (ceiling factors) at the output of the AVR for improved anti-windup performance, replacing the constant saturation settings, and estimate the firing angle directly from the desired field voltage, yielding a direct dynamic relation between the desired and the actual output;
3) Utilize more of the available ceiling voltage with online estimation of the zero crossing depending on the loading condition, replacing the non-direct transfer functions for corrective zero crossing estimation.

The proposed CFR control scheme and the application of the AVM relationships are the main highlights in this contribution. In addition, the proposed AVM is of fundamental importance to determine the overall transfer function of the HSRBES. A future research item is to extend the proposed AVM into a standardized model that can be incorporated into industry standards such as IEEE 421.5 [**?**]. Moreover, a model predictive control (MPC) strategy can be investigated using the proposed AVM.

REFERENCES

[1] Y. Wu, B. Cai, and Q. Ma, “An online diagnostic method for rotary diode open-circuit faults in brushless exciters,” *IEEE Trans. Energy Convers.*, vol. 33, no. 4, pp. 1677–1685, Dec 2018.
[2] H. K. Bui, N. Bracikowski, M. Hecquet, K. Zappellini, and J. Ducreux, “Simulation of a large power brushless synchronous generator (blsg) with a rotating rectifier by a reluctance network for fault analysis and diagnosis,” *IEEE Trans. Ind. Appl.*, vol. 53, no. 5, pp. 4327–4337, Sept 2017.
[3] E. Rebollo, C. A. Platero, F. Blazquez, and R. Granizo, “Internal sudden short-circuit response of a new hsbds for brushless synchronous machines tested on a 15 mva generator,” *IET Elect. Power Appl.*, vol. 11, no. 4, pp. 495–503, 2017.
[4] V. Madonna, P. Giangrande, and M. Galea, “Electrical power generation in aircraft: review, challenges and opportunities,” *IEEE Trans. Transport. Electrific.*, vol. 4, no. 3, pp. 646–659, 2018.
[5] J. Pang, W. Liu, N. Jiao, J. Wang, and P. Ma, “Calculation of cross-coupling inductance and electromagnetic torque in wound-rotor synchronous starter/generator,” *IEEE Trans. Ind. Electron.*, vol. 66, no. 7, pp. 5115–5123, July 2019.

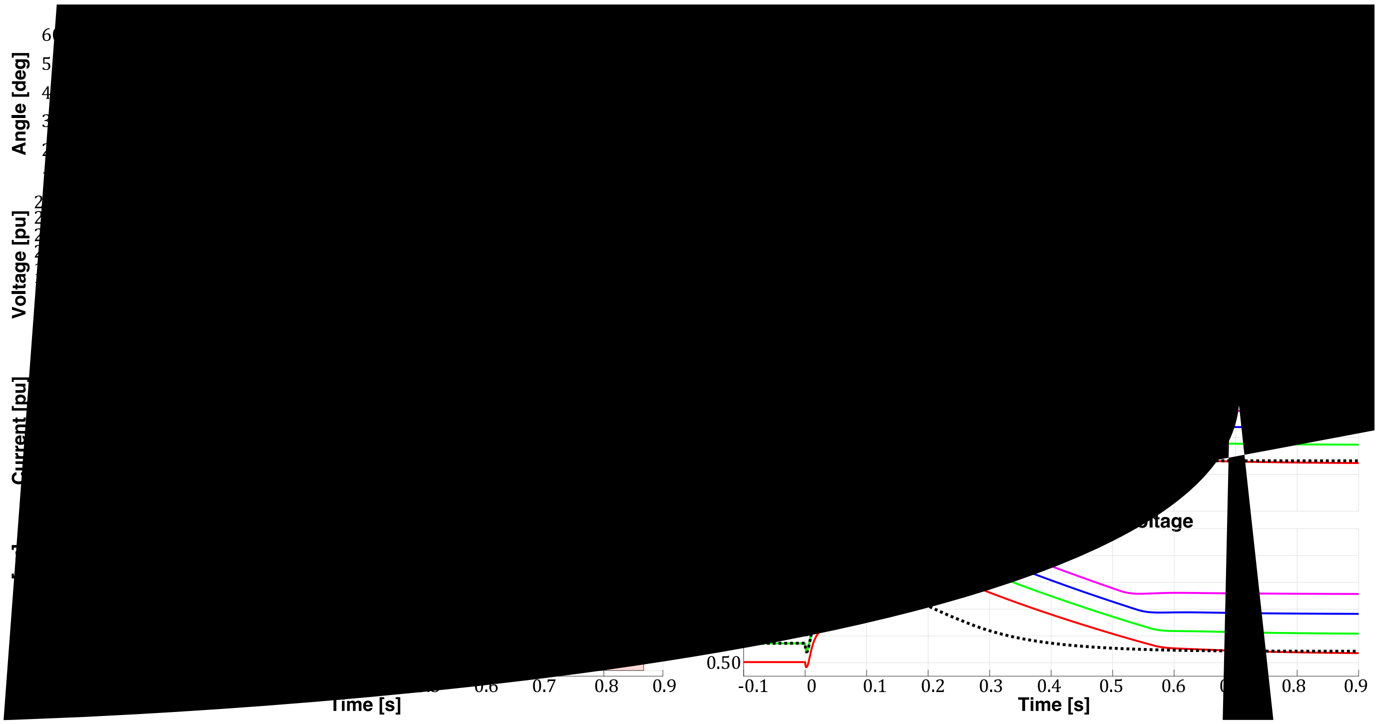

Fig. 21. Comparison between the proposed dual control scheme (CFR) at several set-points versus conventional control based on a fixed exciter field current set-point (FCR). The parameters of the CFR, FCR and the AVR are given in Table V. The table includes a performance comparison.

[6] Y. Zhao, H. Wang, D. Li, and R. Qian, “Comparative research of a wound-field doubly salient generator with different rectifiers,” *IEEE Trans. Ind. Informat.*, vol. 14, no. 11, pp. 4851–4863, Nov 2018.

[7] V. Ruuskanen, M. Niemela, J. Pyrhonen, S. Kanerva, and J. Kaukonen, “Modelling the brushless excitation system for a synchronous machine,” *IET Elect. Power Appl.*, vol. 3, no. 3, pp. 231–239, May 2009.

[8] A. D. Gioia, I. P. Brown, Y. Nie, R. Knippel, D. C. Ludois, J. Dai, S. Hagen, and C. Alteheld, “Design and demonstration of a wound field synchronous machine for electric vehicle traction with brushless capacitive field excitation,” *IEEE Trans. Ind. Appl.*, vol. 54, no. 2, pp. 1390–1403, March 2018.

[9] F. Yao, Q. An, L. Sun, and T. A. Lipo, “Performance investigation of a brushless synchronous machine with additional harmonic field windings,” *IEEE Trans. Ind. Electron.*, vol. 63, no. 11, pp. 6756–6766, Nov 2016.

[10] S. Nuzzo, M. Galea, C. Gerada, and N. Brown, “Analysis, modeling, and design considerations for the excitation systems of synchronous generators,” *IEEE Trans. Ind. Electron.*, vol. 65, no. 4, pp. 2996–3007, April 2018.

[11] T. R. Yalla, C. Chakraborty, and S. Basak, “Brushless induction excited synchronous generator with induction machine operating in plugging mode,” *IEEE Trans. Ind. Appl.*, vol. 54, no. 6, pp. 5748–5759, 2018.

[12] J. Dai, S. Hagen, D. C. Ludois, and I. P. Brown, “Synchronous generator brushless field excitation and voltage regulation via capacitive coupling through journal bearings,” *IEEE Trans. Ind. Appl.*, vol. 53, no. 4, pp. 3317–3326, July 2017.

[13] G. Shrestha, D. Tremelling, W. Arshad, W. Ouyang, and J. Westerlund, “Systems and methods concerning exciterless synchronous machines,” Jan. 16 2015, US Patent App. 14/598,926.

[14] J. K. Nøland, F. Evestedt, J. J. Perez-Loya, J. Abrahamsson, and U. Lundin, “Testing of active rectification topologies on a six-phase rotating brushless outer pole PM exciter,” *IEEE Trans. Energy Convers.*, vol. 33, no. 1, pp. 59–67, March 2018.

[15] K. Röck, “The hydropower plant’s ”ear”: Landsvirkjun and Voith launch joint pilot project in Iceland,” Apr. 2018. [Online]. Available: http://voith.com/corp-en/news-room___press-releases_102767.html

[16] Voith, “Maintenance Free Exciter,” 2013. [Online]. Available: http://voith.com/br/t3383_Maintenance_Free_Exciter_screen.pdf

[17] “Ieee recommended practice for excitation system models for power system stability studies,” *IEEE Std 421.5-2016 (Revision of IEEE Std 421.5-2005)*, pp. 1–207, Aug 2016.

[18] H. Atighechi, S. Chiniforoosh, K. Tabarraee, and J. Jatskevich, “Average-value modeling of synchronous-machine-fed thyristor-controlled-rectifier systems,” *IEEE Trans. Energy Convers.*, vol. 30, no. 2, pp. 487–497, June 2015.

[19] S. Ebrahimi, N. Amiri, H. Atighechi, L. Wang, and J. Jatskevich, “Verification of parametric average-value model of thyristor-controlled rectifier systems for variable-frequency wind generation systems,” *IEEE Trans. Energy Convers.*, vol. 31, no. 1, pp. 401–403, March 2016.

[20] Y. Huang, S. Ebrahimi, N. Amiri, Z. Shan, and J. Jatskevich, “Parametric dynamic phasor modeling of thyristor-controlled rectifier systems including harmonics for various operating modes,” *IEEE Trans. Energy Convers.*, vol. 32, no. 4, pp. 1626–1629, Dec 2017.

[21] S. Ebrahimi, N. Amiri, H. Atighechi, Y. Huang, L. Wang, and J. Jatskevich, “Generalized parametric average-value model of line-commutated rectifiers considering ac harmonics with variable frequency operation,” *IEEE Trans. Energy Convers.*, vol. 33, no. 1, pp. 341–353, March 2018.

[22] M. Shahnazari and A. Vahedi, “Improved dynamic average modelling of brushless excitation system in all rectification modes,” *IET Elect. Power Appl.*, vol. 4, no. 8, pp. 657–669, Sept 2010.

[23] Y. Zhang and A. M. Cramer, “Numerical average-value modeling of rotating rectifiers in brushless excitation systems,” *IEEE Trans. Energy Convers.*, vol. 32, no. 4, pp. 1592–1601, Dec 2017.

[24] ——, “Formulation of rectifier numerical average-value model for direct interface with inductive circuitry,” *IEEE Trans. Energy Convers.*, pp. 1–9, 2018.

[25] N. Jiao, W. Liu, Z. Zhang, T. Meng, J. Peng, and Y. Jiang, “Field current estimation for wound-rotor synchronous starter generator with asynchronous brushless exciters,” *IEEE Trans. Energy Convers.*, vol. 32, no. 4, pp. 1554–1561, Dec 2017.

[26] J. K. Nøland, F. Evestedt, J. J. Pérez-Loya, J. Abrahamsson, and U. Lundin, “Comparison of thyristor rectifier configurations for a six-phase rotating brushless outer pole pm exciter,” *IEEE Trans. Ind. Electron.*, vol. 65, no. 2, pp. 968–976, Feb 2018.

[27] J. K. Nøland, F. Evestedt, and U. Lundin, “Failure-modes demonstration and redundant postfault operation of rotating thyristor rectifiers on brushless dual-star exciters,” *IEEE Trans. Ind. Electron.*, vol. 66, no. 2, pp. 842–851, 2019.

[28] S. Valiviita, “Zero-crossing detection of distorted line voltages using 1-b measurements,” *IEEE Trans. Ind. Electron.*, vol. 46, no. 5, pp. 917–922, Oct 1999.

[29] G. Uicich, M. Benedetti, and J. F. Rovira, “A novel synchronism method for thyristor power converters using the space vector approach,” *IEEE Trans. Nuclear Science*, vol. 53, no. 3, pp. 1522–1529, June 2006.

[30] C. Demoulias and K. Gouramanis, “Voltage multiple-zero-crossings at buses feeding large triac-controlled loads,” *IEEE Trans. Ind. Electron.*, vol. 54, no. 5, pp. 2853–2863, Oct 2007.